WL-TR-96-1143

HIGH RESOLUTION IMAGE RECONSTRUCTION

HIGH RESOLUTION IMAGE RECONSTRUCTION FROM A
SEQUENCE OF ROTATED AND TRANSLATED FRAMES

DR. RUSSELL HARDIE


DEPARTMENT OF ELECTRICAL ENGINEERING
UNIVERSITY OF DAYTON
300 COLLEGE PARK AVE
DAYTON OH 45469

SEPTEMBER 1996

FINAL REPORT FOR 06/01/96-09/01/96
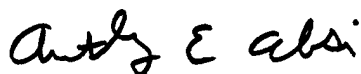
**19961125 009**

# NOTICE

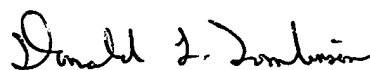WHEN GOVERNMENT DRAWINGS, SPECIFICATIONS, OR OTHER DATA ARE USED FOR ANY PURPOSE OTHER THAN IN CONNECTION WITH A DEFINITELY GOVERNMENT-RELATED PROCUREMENT, THE UNITED STATES GOVERNMENT INCURS NO RESPONSIBILITY OF ANY OBLIGATION WHATSOEVER. THE FACT THAT THE GOVERNMENT MAY HAVE FORMULATED OR IN ANY WAY SUPPLIED THE SAID DRAWINGS, SPECIFICATIONS, OR OTHER DATA, IS NOT TO BE REGARDED BY IMPLICATION, OR OTHERWISE IN ANY MANNER CONSTRUED, AS LICENSING THE HOLDER, OR ANY OTHER PERSON OR CORPORATION; OR AS CONVEYING ANY RIGHTS OR PERMISSION OT MANUFACTURE, USE, OR SELL ANY PATENTED INVENTION THAT MAY IN ANY WAY BE RELATED THERETO.
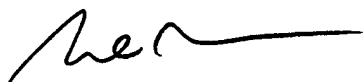
THIS TECHNICAL REPORT HAS BEEN REVIEWED AND IS APPROVED FOR PUBLICATION.

ANTHONY E. ABSI, PROJECT ENGINEER
EO SENSOR TECHNOLOGY BRANCH
EO DIVISION

DONALD L. TOMLINSON, Chief
Technology Branch
Electro-Optics Division

FOR THE COMMANDER

WILLIAM J. CANNON, Chief
Electro-Optics Division
Avionics Directorate

IF YOUR ADDRESS HAS CHANGED, IF YOU WISH TO BE REMOVED FROM OUR MAILING LIST, OR IF THE ADDRESSEE IS NO LONGER EMPLOYED BY YOUR ORGANIZATION, PLEASE NOTIFY WL/AAJT, BLDG 622, 3109 P ST, WRIGHT-PATTERSON AFB OH 45433-7700 TO HELP MAINTAIN A CURRENT MAILING LIST.

COPIES OF THIS REPORT SHOULD NOT BE RETURNED UNLESS RETURN IS REQUIRED BY SECURITY CONSIDERATIONS, CONTRACTUAL OBLIGATIONS, OR NOTICE ON A SPECIFIC DOCUMENT.

# REPORT DOCUMENTATION PAGE

*Form Approved*
*OMB No. 0704-0188*

| 1. AGENCY USE ONLY *(Leave blank)* | 2. REPORT DATE<br>SEP 1996 | 3. REPORT TYPE AND DATES COVERED<br>FINAL 06/01/96--09/01/96 |
|---|---|---|

| 4. TITLE AND SUBTITLE HIGH RESOLUTION IMAGE RECONSTRUCTIO<br><br>HIGH RESOLUTION IMAGE RECONSTRUCTION FROM A SEQUENCE OF ROTATED AND TRANSLATED FRAMES | 5. FUNDING NUMBERS<br><br>PE 61102<br>PR 2300 |
|---|---|

**6. AUTHOR(S)** DR. RUSSELL HARDIE

TA AA
WU 13

| 7. PERFORMING ORGANIZATION NAME(S) AND ADDRESS(ES)<br><br>AVIONICS DIRECTORATE<br>WRIGHT LABORATORY<br>AIR FORCE MATERIEL COMMAND<br>WRIGHT PATTERSON AFB OH 45433-7623 | 8. PERFORMING ORGANIZATION REPORT NUMBER |
|---|---|

| 9. SPONSORING/MONITORING AGENCY NAME(S) AND ADDRESS(ES)<br><br>AVIONICS DIRECTORATE<br>WRIGHT LABORATORY<br>AIR FORCE MATERIEL COMMAND<br>WRIGHT PATTERSON AFB OH 45433-7623<br>(POC: Tony Absi, Sensor Tech Branch, phone: 937-255-9614) | 10. SPONSORING/MONITORING AGENCY REPORT NUMBER<br><br>WL-TR-96-1143 |
|---|---|

**11. SUPPLEMENTARY NOTES**

| 12a. DISTRIBUTION/AVAILABILITY STATEMENT<br><br>APPROVED FOR PUBLIC RELEASE; DISTRIBUTION IS UNLIMITED. | 12b. DISTRIBUTION CODE |
|---|---|

**13. ABSTRACT** *(Maximum 200 words)* Some imaging sytems employ detector arrays which are not dense enough to meet the Nyquist criteria during image acquisition. This is particularly true for many staring infrared imagers. Thus, the full resolution afforded by the optics is not being realized in such a system. This paper presents a technique for estimating a high resolution image, with reduced aliasing, from a sequence of undersampled rotated and translationally shifted frames. Such an image sequence can can be obtained if an imager is mounted on a moving platform, such as an aircraft. Several approaches to this problem have been proposed in the literature. Here we extend some of this previous work. In particular, we define an observation model which incorporates accurate knowledge of the optical system. The high resolution image estimate is formed by minimizing a regularized cost function which is based on the observation model. We consider both gradient descent and conjugate gradiend optimization procedures to minimize the cost function. We show that the conjugate gradient optimization provides rapid convergence. Detailed experimental results are provided to illustrate the performance of the proposed algorithm using both visible and infrared images. Quantitative error analysis is provided and several images are shown for subjective evaluation.

| 14. SUBJECT TERMS<br><br>IMAGE ENHANCEMENT, INFRARED, IMAGING PROCESSING, INFRARED SENSORS | 15. NUMBER OF PAGES<br>33 |
|---|---|
| | 16. PRICE CODE |

| 17. SECURITY CLASSIFICATION OF REPORT<br>UNCLASSIFIED | 18. SECURITY CLASSIFICATION OF THIS PAGE<br>UNCLASSIFIED | 19. SECURITY CLASSIFICATION OF ABSTRACT<br>UNCLASSIFIED | 20. LIMITATION OF ABSTRACT<br>SAR |
|---|---|---|---|

# Contents

# List of Tables

# List of Figures

iv

# 1 Introduction

In imaging systems where the focal plane detector array is not sufficiently dense, so as to meet the Nyquist criterion, the resulting images will be degraded by aliasing effects. This undersampling is a common problem among staring infrared imaging systems. This is due to fabrication complexities and quantum efficiency problems associated with manufacturing small and dense infrared focal plane arrays (FPAs). While it is possible to equip such systems with optics to properly bandlimit the input, this generally means employing optics with a very small instantaneous field of view (IFOV). This may be highly undesirable in some applications. Furthermore, inexpensive charge coupled device (CCD) cameras may also employ detector arrays which are not sufficiently dense for the desired optics. Thus, the goal of this work is to obtain high resolution images, with reduced aliasing, from such systems. In addition, we wish to remove the blurring effects of the finite size detectors and the optics.

One way to overcome the undersampling problem, without low pass filtering the input or sacrificing IFOV, is to exploit multiple frames from an image sequence. This is possible if there is relative motion between the scene and the FPA during image sequence acquisition. In this case, a unique "look" at the scene (i.e., a unique set of samples) may be provided by each frame. The desired image sequence can be obtained if an imager is mounted on a moving platform, such as an aircraft. We refer to this as uncontrolled microscanning [1]. It is also possible to introduce a controlled mirror in the optical path to translate the scene intensity image across the FPA. This is referred to as controlled microscanning [1, 2]. Here we focus on uncontrolled microscanning and we consider both rotational and translational motion of the scene relative to the FPA. The key to the high resolution image recovery algorithm is accurate knowledge of the sub-pixel translation and rotation of each frame. If these parameters are unknown, as in the uncontrolled case, they must be estimated from the observed images. Thus, we must consider both image registration and high resolution image reconstruction.

Several approaches to the high resolution image reconstruction problem have been proposed in the literature. One of the first techniques proposed seeks to solve for an unaliased discrete spectrum by solving a set of frequency domain linear equations [3].

This approach has been extended to treat noise in [4] and blur in [5]. These techniques, however, do not address rotation which may be present in many applications. Furthermore, we have found that they tend to be highly sensitive to errors in the registration parameters. This is particularly true when attempting to remove blur [5].

Another approach to the high resolution image reconstruction problem uses a projection onto convex sets (POCS) algorithm [6]. The POCS approach has been extended to treat motion blur and noise in [7, 8]. The problem has also been approached from a statistical estimation framework. Specifically, a maximum *a posteriori* (MAP) estimator is developed in [9, 10] which is an extension of a single frame image expansion algorithm proposed in [11]. A statistical estimation approach was first applied to forward looking infrared (FLIR) data in [12]. In particular, a maximum likelihood technique using the expectation maximization (EM) algorithm is developed which seeks to jointly estimate the translational shifts and a high resolution image [12]. In addition, a joint registration and high resolution reconstruction technique using MAP estimation is presented in [13]. The work in [12] and [13] does not explicitly treat the case of rotational motion. Another related MAP approach can be found in [14].

The reconstruction algorithm presented here can be viewed as an extension of the basic approach presented in [15]. The technique in [15] seeks to minimize a specified cost function using an iterative algorithm. This cost function is the total squared error between the observed low resolution data and the predicted low resolution data. The predicted data is the result of projecting the high resolution image estimate through the observation model. Here we employ the same registration technique used in [15] and we seek to minimize a related cost function. However, our approach includes a number of important and fundamental differences. Some of the novel aspects of the work presented here are as follows:

- The observation model uses accurate information about the optical system to form a realistic point spread function (PSF). In particular, the PSF model is defined to include the effects of the optics and the finite size detectors.

- The cost function defined here includes a regularization term. This extra term adds robustness, particularly when only a small number of frames are available or when

then the fidelity of the data is low.

- The unconstrained minimization of the cost function is achieved using a gradient descent and a conjugate gradient technique. The conjugate gradient technique, in particular, provides rapid convergence.

- Finally, we study the application of high resolution image reconstruction to a real-time infrared imaging system.

The organization of the rest of the paper is as follows. In Section 2, the observation model is described. Both a continuous and discrete model are developed. Section 3 addresses image registration. The high resolution image reconstruction algorithm is developed in Section 4. In particular, the regularized cost function is defined and two optimization procedures are described. Experimental results are provided in Section 5. These include results obtained using simulated data and using FLIR images acquired from a real-time system. Quantitative error analysis is provided and several images are shown for subjective evaluation. Finally, some conclusions are given in Section 6.

# 2 Observation Model

In this section, the observation model is presented. This model is the basis for the high resolution reconstruction algorithm developed in Section 4. We begin with a continuous model which closely follows the physical image acquisition process. An equivalent discrete model is then presented. It is the discrete model which is utilized in the reconstruction algorithm. We conclude this section with the characterization of the system point spread function, since this represents a key element in the observation model.

## 2.1 Continuous Model

A block diagram of the continuous observation model is shown in Fig. 1. The true scene intensity image is defined as $o(x, y)$. The motion of the imager that occurs between image acquisitions is modeled as a pure rotation and translation of the scene intensity image. For a moving imager and a stationary scene in the far field, this is a fairly

3
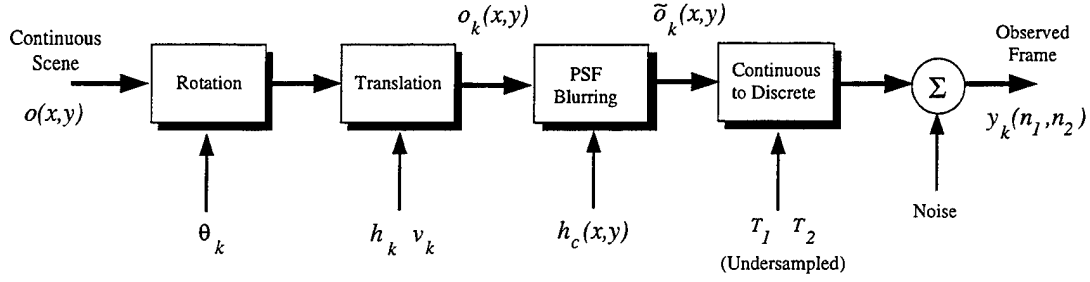
Figure 1: Continuous observation model resembling the physical process of image acquisition.

accurate model, since occlusion effects and perspective changes are minimal. Thus, the $k$'th observed frame in a sequence can be expressed as

$$o_k(x, y) = o(x\cos\theta_k - y\sin\theta_k + h_k, y\cos\theta_k + x\sin\theta_k + v_k), \tag{1}$$

for $k = 1, 2, 3, \ldots, p$. Note that $\theta_k$ represents the rotation of the $k$'th frame about the origin (i.e., $x = 0$, $y = 0$). The parameters $h_k$ and $v_k$ represent the horizontal and vertical shift associated with the $k$'th frame.

The blurring effect of the optics and finite detector size is modeled by a convolution operation yielding

$$\tilde{o}_k(x, y) = o_k(x, y) * h_c(x, y), \tag{2}$$

where $h_c(x, y)$ is the continuous system PSF. More will be said about the PSF in Section 2.3. Finally, the blurred, rotated and translated image is sampled below the Nyquist rate and corrupted by noise. This yields the $k$'th low resolution observed frame

$$y_k(n_1, n_2) = \tilde{o}_k(n_1 T_1, n_2 T_2) + \eta_k(n_1, n_2), \tag{3}$$

where $T_1$ and $T_2$ are the horizontal and vertical sample spacings and $\eta_k(n_1, n_2)$ is an additive noise term. Let the dimensions of the low resolution image $y_k(n_1, n_2)$ be $N_1 \times N_2$. These data in lexicographical notation will be expressed as $\mathbf{y}_k = [y_{k,1}, y_{k,2}, \ldots, y_{k,M}]^T$, where $M = N_1 N_2$. Finally, let the full set of $p$ observed low resolution images be denoted

$$\mathbf{y} = [\mathbf{y}_1^T, \mathbf{y}_2^T, \ldots, \mathbf{y}_p^T]^T = [y_1, y_2, \ldots, y_{pM}]^T. \tag{4}$$

Thus, all observed pixel values are contained within $\mathbf{y}$.

4

Figure 2: Equivalent discrete observation model illustrating the relationship between the ideally sampled image z and the observed frames y.

## 2.2 Discrete Model

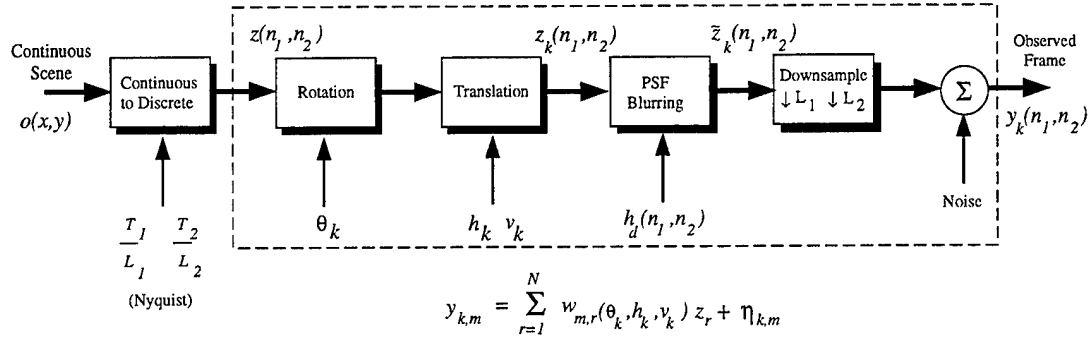While the continuous model provides insight into the physical process, we require a discrete observation model to develop the high resolution reconstruction algorithm. That is, we need a model relating a discrete high resolution image to the low resolution observed frames y. Figure 2 illustrates such a discrete model which is equivalent to that in Fig. 1. The difference here is that we first define $z(n_1, n_2)$ to be an intensity image sampled at or above the Nyquist rate with no blur or noise degradation. It is this discrete image we wish to estimate from the observed frames. Let this high resolution image be of size $L_1 N_1 \times L_2 N_2 = N$, where $L_1$ and $L_2$ are positive integers. More will be said about these parameters shortly. In later analysis it will be convenient to express this image in lexicographical notation as the vector $\mathbf{z} = [z_1, z_2, \ldots, z_N]^T$.

As before, this image is rotated by $\theta_k$ and shifted by $h_k$ and $v_k$ producing $z_k(n_1, n_2)$. Here we will define the shifts $h_k$ and $v_k$ in terms of low resolution pixel spacings for convenience. Note that this step requires interpolation since the sampling grid changes in the geometric transformation. Theoretically, one could use ideal interpolation since $z(n_1, n_2)$ is defined to be sampled above the Nyquist rate. However, in practice, simpler interpolation methods such as nearest neighbor and bilinear interpolation can be used [16]. For large values of $L_1$ and $L_2$, the high resolution grid is so dense that simple interpolation methods can be reasonably accurate.

Next, the system PSF is accounted for yielding

$$\tilde{z}(n_1, n_2) = z_k(n_1, n_2) * h_d(n_1, n_2), \tag{5}$$

5

where $h_d(n_1, n_2)$ is the equivalent discrete system PSF. Note that the blurring is performed after the geometric transformation. If the PSF is circularly symmetric, then the blurring can be equivalently introduced prior to the rotation. This saves on computations since the blurring is performed only once in this case. Finally, the transformed image is subsampled down to the resolution of the observed frames yielding

$$y_k(n_1, n_2) = z_k(n_1 L_1, n_2 L_2) + \eta_k(n_1, n_2). \tag{6}$$

Aliasing is generally introduced in this final step.

This discrete model can be rewritten in a simple form where the low resolution pixels are defined as a weighted sum of the appropriate high resolution pixels with additive noise. This generalized form can account for the PSF blurring, the geometric transformation and the subsampling of the high resolution image. Specifically, the observed low resolution pixels from frame $k$ are related to the high resolution image as follows

$$y_{k,m} = \sum_{r=1}^{N} w_{m,r}(\theta_k, h_k, v_k) z_r + \eta_{k,m}, \tag{7}$$

for $m = 1, 2, \ldots, M$ and $k = 1, 2, \ldots, p$. The weight $w_{m,r}(\theta_k, h_k, v_k)$ represents the "contribution" of the $r$'th high resolution pixel to the $m$'th low resolution observed pixel of the $k$'th frame. The parameters $\theta_k$, $h_k$ and $v_k$ represent the rotation, horizontal and vertical translational shifts, respectively, of the $k$'th frame with respect to some reference on the high resolution grid. The term $\eta_{k,m}$ in (7) represents an additive noise sample. To further compact the notation, the model in (7) can be expressed in terms of the entire set of low resolution pixels as

$$y_m = \sum_{r=1}^{N} w_{m,r} z_r + \eta_m, \tag{8}$$

for $m = 1, 2, \ldots, pM$ and where $w_{m,r}$ is simply the contribution of the $r$'th high resolution pixel in $\mathbf{z}$ to the $m$'th low resolution pixel in $\mathbf{y}$. It is assumed that the underlying scene, $\mathbf{z}$, remains constant during the acquisition of the multiple low resolution frames. Furthermore, we assume here that the only frame to frame differences in the weights result from rotation and translational of each low resolution frame relative to the high resolution grid.

$$(a) \qquad\qquad (b)$$
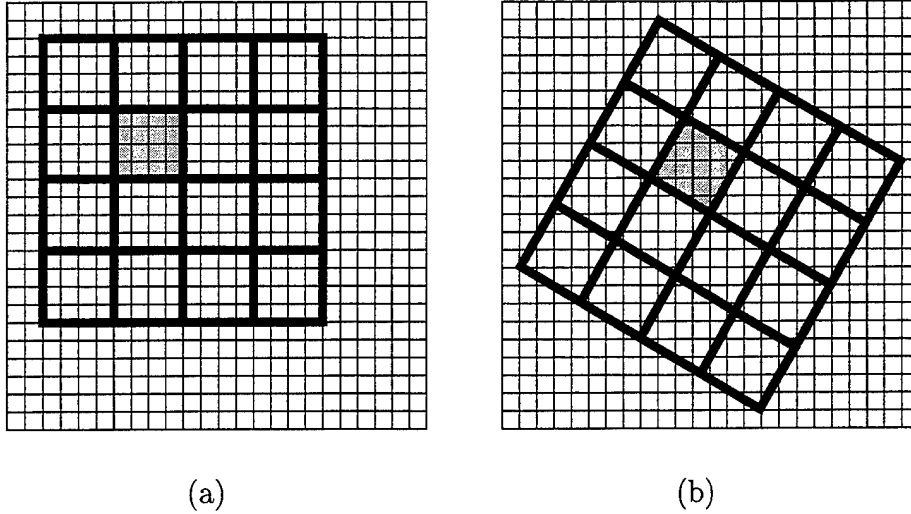
Figure 3: Discrete detector model showing those high resolution pixels that contribute to a low resolution pixel for two different registration positions.

A simple way to visualize the form of the observation model in (8) is to consider only the blur from the finite detector size. This scenario is illustrated in Fig. 3. Here each low resolution pixel is obtained by summing the high resolution pixels within the span of that low resolution detector. One low resolution detector in Fig. 3(a) is shaded to illustrate this point. This discrete detector model simulates the integration of light intensity that falls within the span of the low resolution detector. As the low resolution grid shifts relative to the fixed high resolution grid, as in Fig. 3(b), a different set of high resolution pixels contribute to each low resolution pixel. This yields a new set of linearly independent equations from (8). Clearly, some type of interpolation is required for any non-integer shift on the high resolution grid or any non-trivial rotation. This interpolation can be accounted for by modifying the weights in (8). This simple detector model can give good results. However, a more realistic PSF model is described in the following section.

## 2.3 System Point Spread Function

For most systems, there are two main contributors to the system PSF. The primary contributor is generally the finite detector size as illustrated in Fig. 3. This effect is spatially invariant for a uniform detector array. The second contributor is the optics. Here we assume an isoplanatic model for the optics [17]. We derive and use a theoretical PSF because, for the type of systems considered in this paper, direct measurement of an *unaliased* system PSF is not possible.

Let us begin by considering a system with a uniform detector array. The effect of the integration of light intensity over the span of the detectors can be modeled as a linear convolution operation with a PSF determined by the geometry of a single detector. Let this PSF be denoted $d(x, y)$. Applying the Fourier transform to $d(x, y)$ yields the effective continuous frequency response resulting from the detectors

$$D(u, v) = \mathcal{FT}\{d(x, y)\}, \tag{9}$$

where $\mathcal{FT}\{\cdot\}$ represents the continuous Fourier transform. Next, define the incoherent optical transfer function (OTF) of the optics to be $H_o(u, v)$. The overall system OTF is given by the product of these, yielding

$$H(u, v) = D(u, v)H_o(u, v). \tag{10}$$

The overall continuous system PSF is then given by

$$h(x, y) = \mathcal{FT}^{-1}\{H(u, v)\}, \tag{11}$$

where $\mathcal{FT}^{-1}\{\cdot\}$ represents the inverse Fourier transform. Finally, the impulse-invariant discrete system PSF [18] on the high resolution grid is obtained by sampling the continuous PSF such that

$$h_d(n_1, n_2) = \frac{T_1 T_2}{L_1 L_2} h\left(\frac{n_1 T_1}{L_1}, \frac{n_2 T_2}{L_2}\right). \tag{12}$$

This accurately represents the continuous blurring when the effective sampling frequency $L_1/T_1$ exceeds two times the horizontal cutoff frequency of $H(u, v)$ and $L_2/T_2$ exceeds two times the vertical cutoff frequency [18].

Let us now specifically consider a system with uniform rectangular detectors. An illustration of such a detector array with critical dimensions labeled is provided in Fig.
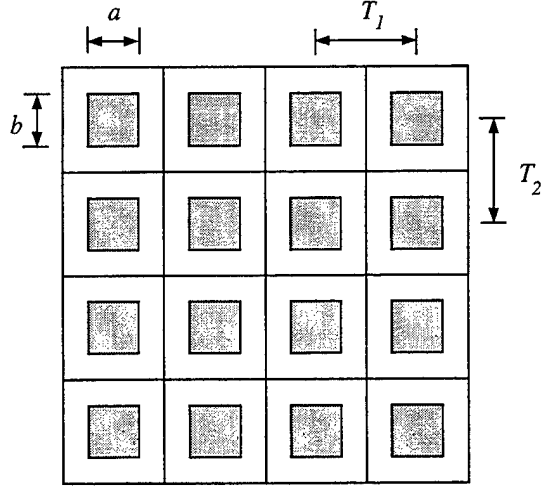
Figure 4: Uniform detector array illustrating critical dimensions.

4. The shaded areas represent the active region of each detector. The detector model PSF in this case is given by

$$d(x, y) = \frac{1}{ab}\text{rect}\left(\frac{x}{a}, \frac{y}{b}\right) = \begin{cases} 1 & \text{for } |x/a| < 1/2 \text{ and } |x/b| < 1/2 \\ 0 & \text{otherwise} \end{cases}. \tag{13}$$

Let the active region dimensions, $a$ and $b$, be measured in millimeters (mm). Thus, the effective continuous frequency response resulting from the detectors is

$$D(u, v) = \text{sinc}(au, bv) = \frac{\sin(\pi au)\sin(\pi bv)}{\pi^2 aubv}, \tag{14}$$

where $u$ and $v$ are the horizontal and vertical frequencies measured in cycles/mm.

The incoherent optical transfer function (OTF) of diffraction-limited optics with a circular exit pupil can be found [17] as

$$H_o(u, v) = \begin{cases} \frac{2}{\pi}[\cos^{-1}\left(\frac{\rho}{\rho_c}\right) - \frac{\rho}{\rho_c}\sqrt{1 - \left(\frac{\rho}{\rho_c}\right)^2}] & \text{for } \rho < \rho_c \\ 0 & \text{otherwise} \end{cases}, \tag{15}$$

where $\rho = \sqrt{u^2 + v^2}$. The parameters $\rho_c$ is the radial system cutoff frequency given by

$$\rho_c = \frac{1}{\lambda f/\#}, \tag{16}$$

where $f/\#$ is the f-number of the optics and $\lambda$ is the wavelength of light considered. Since the cutoff of $H_o(u, v)$ is $\rho_c$, so is the cutoff of the overall system $H(u, v)$. Thus, the

9

impulse-invariant discrete system defined in (12) will accurately model the continuous system when $L_1 \geq \lceil 2\rho_c T_1 \rceil$ and $L_2 \geq \lceil 2\rho_c T_2 \rceil$. This choice of $L_1$ and $L_2$ also defines a high resolution sampling grid at or above the Nyquist rate for an arbitrary scene. That is, the effective high resolution sampling rates of $L_1/T_1$ and $L_2/T_2$ will be more than twice the OTF cutoff frequency.

Figure 5 shows an example of $D(u,v)$, $H_o(u,v)$, $H(u,v)$ and $h_c(x,y)$ for a particular imaging system. The system considered is the FLIR imager used to collect data for the experimental results presented in Section 5. The FLIR camera uses a $128 \times 128$ Amber AE-4128 infrared FPA. The FPA is composed of Indium-Antimonide (InSb) detectors with a response in the $3\mu m$ - $5\mu m$ wavelength band. This system has square detectors of size $a = b = .040$mm. The imager is equipped with 100mm $f/3$ optics. The center wavelength, $\lambda = .004$mm, is used in the OTF calculation. Figure 5(a) shows the effective modulation transfer function (MTF) of the detectors, $|D(u,v)|$. The diffraction-limited OTF for the optics, $H_o(u,v)$, is shown in Fig. 5(b). Note that the cutoff frequency is 83.3 cycles/mm. The overall system MTF, $|H(u,v)|$, is plotted in Fig. 5(c). Finally, the continuous system PSF, $h_c(x,y)$, is plotted in Fig. 5(d).

The detector spacing on the Amber FPA is $T_1 = T_2 = .050$mm, yielding a sampling frequency of 20 cycles/mm in both directions. Thus, the effective sampling rate must be increased by a factor of 8.33 to eliminate aliasing entirely for an arbitrary scene. This would require that we select $L_1$, $L_2 \geq 9$. In practice, we find that good results can be obtained with smaller values of $L_1$ and $L_2$.

# 3  Image Registration

In most applications, the registration parameters in the observation model, $\theta_k$, $h_k$ and $v_k$, will not be known *a priori*. Thus, they must be estimated from the observed image sequence. Accurate sub-pixel registration is the key to the success of the high resolution image reconstruction algorithm. A number of image registration techniques have been proposed in the literature. We have found that a practical and effective method of estimating the sub-pixel translation and rotation is using the technique in [15], which is based on that in [19]. For convenience, this algorithm is presented here using the current
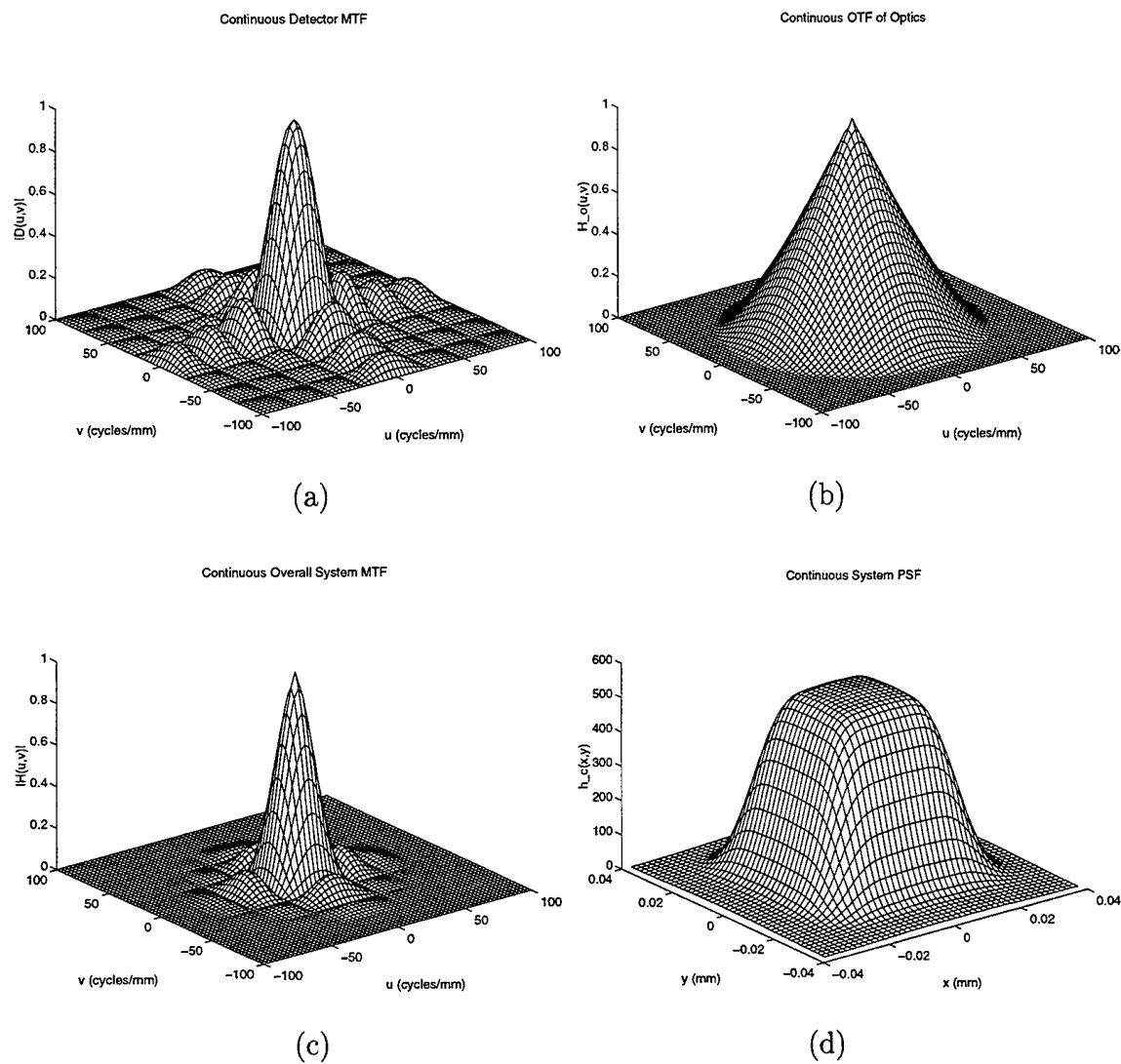
Figure 5: (a) Effective MTF of the detectors in the FLIR imager (b) diffraction-limited OTF of the optics (c) overall system MTF (d) overall continuous system PSF.

11

notation.

To begin, define the first observed frame to be the reference frame and without loss of generality let $\theta_1 = h_1 = v_1 = 0$. According to our model,

$$o_k(x,y) = o_1(x\cos\theta_k - y\sin\theta_k + h_k, y\cos\theta_k + x\sin\theta_k + v_k), \qquad (17)$$

for $k = 2, 3, \ldots, p$. Note that this assumes that the center of rotation is at the origin (i.e., $x = 0$, $y = 0$). This is not restrictive however, since we allow any shift $h_k$ and $v_k$. If the PSF blur is approximately circularly symmetric, then

$$\tilde{o}_k(x,y) \approx \tilde{o}_1(x\cos\theta_k - y\sin\theta_k + h_k, y\cos\theta_k + x\sin\theta_k + v_k). \qquad (18)$$

For very small values of $\theta_k$, we can make the following approximations: $\sin\theta_k \approx \theta_k$ and $\cos\theta_k \approx 1$. Using these yields

$$\tilde{o}_k(x,y) \approx \tilde{o}_1(x - y\theta_k + h_k, y + x\theta_k + v_k). \qquad (19)$$

Now we use the first three terms of the Taylor series expansion as an approximation for the right side in (19). This yields

$$\tilde{o}_k(x,y) \approx \tilde{o}_1(x,y) + (h_k - y\theta_k)g_x(x,y) + (v_k + x\theta_k)g_y(x,y), \qquad (20)$$

where $g_x(x,y) = \frac{\partial \tilde{o}_1(x,y)}{\partial x}$ and $g_y(x,y) = \frac{\partial \tilde{o}_1(x,y)}{\partial y}$.

In light of the relationship expressed in (20), we define the least squares estimates for the registration parameters as follows

$$\hat{\theta}_k, \ \hat{h}_k, \ \hat{v}_k = \frac{\arg \min}{\theta_k, \ h_k, \ v_k} \ E_k(\theta_k, \ h_k, \ v_k), \qquad (21)$$

where

$$E_k(\theta_k, \ h_k, \ v_k) = \sum_{(x,y)\in S} (\tilde{o}_k(x,y) - \tilde{o}_1(x,y) - (h_k - y\theta_k)g_x(x,y) - (v_k + x\theta_k)g_y(x,y))^2. \qquad (22)$$

Note that $S$ represents the grid of points in the $R^2$ space, defined by $x$ and $y$, at which we have discrete samples. Rewriting this error in terms of the observed images yields

$$E_k(\theta_k, \ h_k, \ v_k) = \sum_{\mathbf{n}\in\mathcal{N}} (y_k(\mathbf{n}) - y_1(\mathbf{n}) - (h_k - n_2 T_2 \theta_k)\hat{g}_x(\mathbf{n}) - (v_k + n_1 T_1 \theta_k)\hat{g}_y(\mathbf{n}))^2, \qquad (23)$$

12

where $\mathbf{n} = [n_1, n_2]$ and $\mathcal{N}$ is the set of indices on the low resolution discrete grid for which we have observations. Note that the center of rotation on the discrete grid is assumed to be at $n_1 = n_2 = 0$. The functions $\hat{g}_x(\mathbf{n})$ and $\hat{g}_y(\mathbf{n})$ are discrete estimates of $g_x(x, y)$ and $g_y(x, y)$, respectively, at location $x = n_1 T_1$ and $y = n_2 T_2$. These can be computed using scaled Prewitt operators [16], for example.

To solve the minimization problem in (21), we begin by differentiating $E(\theta_k, h_k, v_k)$ with respect to $\theta_k$, $h_k$ and $v_k$ and set the derivatives equal to zero. This yields the following three equations

$$\sum_{\mathbf{n}\in\mathcal{N}} \left( h_k \hat{g}_x^2(\mathbf{n}) + v_k \hat{g}_x(\mathbf{n})\hat{g}_y(\mathbf{n}) + \theta_k \bar{g}(\mathbf{n})\hat{g}_x(\mathbf{n}) \right) = \sum_{\mathbf{n}\in\mathcal{N}} \bar{y}_k(\mathbf{n})\hat{g}_x(\mathbf{n}), \tag{24}$$

$$\sum_{\mathbf{n}\in\mathcal{N}} \left( h_k \hat{g}_x(\mathbf{n})\hat{g}_y(\mathbf{n}) + v_k \hat{g}_y^2(\mathbf{n}) + \theta_k \bar{g}(\mathbf{n})\hat{g}_y(\mathbf{n}) \right) = \sum_{\mathbf{n}\in\mathcal{N}} \bar{y}_k(\mathbf{n})\hat{g}_y(\mathbf{n}), \tag{25}$$

and

$$\sum_{\mathbf{n}\in\mathcal{N}} \left( h_k \bar{g}(\mathbf{n})\hat{g}_x(\mathbf{n}) + v_k \bar{g}(\mathbf{n})\hat{g}_y(\mathbf{n}) + \theta_k \bar{g}^2(\mathbf{n}) \right) = \sum_{\mathbf{n}\in\mathcal{N}} \bar{y}_k(\mathbf{n})\bar{g}(\mathbf{n}), \tag{26}$$

where

$$\bar{g}(\mathbf{n}) = n_1 T_1 \hat{g}_y(\mathbf{n}) - n_2 T_2 \hat{g}_x(\mathbf{n}) \tag{27}$$

and

$$\bar{y}_k(\mathbf{n}) = y_k(\mathbf{n}) - y_1(\mathbf{n}). \tag{28}$$

We then simultaneously solve these expressions. To do so let

$$MR_k = V_k, \tag{29}$$

where

$$M = \begin{bmatrix} \sum_{\mathbf{n}\in\mathcal{N}} \hat{g}_x^2(\mathbf{n}) & \sum_{\mathbf{n}\in\mathcal{N}} \hat{g}_x(\mathbf{n})\hat{g}_y(\mathbf{n}) & \sum_{\mathbf{n}\in\mathcal{N}} \bar{g}(\mathbf{n})\hat{g}_x(\mathbf{n}) \\ \sum_{\mathbf{n}\in\mathcal{N}} \hat{g}_x(\mathbf{n})\hat{g}_y(\mathbf{n}) & \sum_{\mathbf{n}\in\mathcal{N}} \hat{g}_y^2(\mathbf{n}) & \sum_{\mathbf{n}\in\mathcal{N}} \bar{g}(\mathbf{n})\hat{g}_y(\mathbf{n}) \\ \sum_{\mathbf{n}\in\mathcal{N}} \bar{g}(\mathbf{n})\hat{g}_x(\mathbf{n}) & \sum_{\mathbf{n}\in\mathcal{N}} \bar{g}(\mathbf{n})\hat{g}_y(\mathbf{n}) & \sum_{\mathbf{n}\in\mathcal{N}} \bar{g}^2(\mathbf{n}) \end{bmatrix}, \tag{30}$$

$R_k = [h_k, v_k, \theta_k]^T$, and

$$V_k = \begin{bmatrix} \sum_{\mathbf{n}\in\mathcal{N}} \bar{y}_k(\mathbf{n})\hat{g}_x(\mathbf{n}) \\ \sum_{\mathbf{n}\in\mathcal{N}} \bar{y}_k(\mathbf{n})\hat{g}_y(\mathbf{n}) \\ \sum_{\mathbf{n}\in\mathcal{N}} \bar{y}_k(\mathbf{n})\bar{g}(\mathbf{n}) \end{bmatrix}. \tag{31}$$

Finally, the estimated registration vector, $\hat{R}_k = [\hat{h}_k, \hat{v}_k, \hat{\theta}_k]^T$, can be computed as

$$\hat{R}_k = M^{-1} V_k. \tag{32}$$

13

Table 1: Iterative registration algorithm for $y_k(\mathbf{n})$, where $k = 2, 3, \ldots, p$.

---

**step 1**: Compute $\hat{g}_x(\mathbf{n})$, $\hat{g}_y(\mathbf{n})$ and $\bar{g}(\mathbf{n})$ from $y_1(\mathbf{n})$ and form $M$ matrix.

**step 2**: Let $n = 0$, $y_k^0(\mathbf{n}) = y_k(\mathbf{n})$ and $\hat{R}_k^0 = [0, 0, 0]^T$.

**step 3**: Compute $V_k$ using $\bar{y}_k(\mathbf{n}) = y_k^n(\mathbf{n}) - y_1(\mathbf{n})$ and then let $n = n + 1$.

**step 4**: Compute $\hat{R}_k^n = M^{-1}V_k + \hat{R}_k^{n-1}$.

**step 5**: if $||\hat{R}_k^n - \hat{R}_k^{n-1}||/||\hat{R}_k^{n-1}|| < T$, let $\hat{R}_k = \hat{R}_k^n$ and stop.

**step 6**: Resample $y_k(\mathbf{n})$ towards $y_1(\mathbf{n})$ according to $\hat{R}_k^n$ to create $y_k^n(\mathbf{n})$ and go to step 3.

---

To obtain shifts in terms of low resolution pixel spacings (rather than in mm), we set $T_1 = T_2 = 1$ in (27).

Because of the assumptions made, this technique is only accurate for small shifts and rotations. To treat the case where larger values are expected, we follow the iterative method used in [15] and [19]. To do so, the initial registration parameters are estimated according to (32). Next $y_k(\mathbf{n})$ is shifted and rotated according to the registration parameter estimates so as to more closely match $y_1(\mathbf{n})$. This modified image is then registered to $y_1(\mathbf{n})$. The process continues whereby $y_k(\mathbf{n})$ is continually modified until the registration estimates become sufficiently small. The final registration estimate is obtained by summing all of the "partial" estimates. The iterative registration procedure for $y_k(\mathbf{n})$, where $k = 2, 3, \ldots, p$, is summarized in Table 1.

Because the three parameters are well overdetermined by the data, this least squares estimate is generally accurate. We find that the main source of error lies in the resampling of $y_k(\mathbf{n})$ (step 6 in Table 1), since this requires interpolation on the low resolution aliased grid. Some error is also introduced in the discrete gradient estimates. In general, however, the algorithm appears to provide sufficiently accurate results for our current application. In cases where the aliasing is more severe, a joint registration and recon-

struction algorithm, like that described in [12], [14], and [13], may be advantageous.

# 4 High Resolution Image Reconstruction

With estimates of the registration parameters, the observation model can be completely specified. In light of the observation model in (8), we define the high resolution image estimate to be

$$\hat{\mathbf{z}} = \overset{\arg\min}{\mathbf{z}} \ C(\mathbf{z}), \tag{33}$$

where

$$C(\mathbf{z}) = \frac{1}{2} \sum_{m=1}^{pM} \left( y_m - \sum_{r=1}^{N} w_{m,r} z_r \right)^2 + \frac{\lambda}{2} \sum_{i=1}^{N} \left( z_i - \sum_{j=1}^{N} \alpha_{i,j} z_j \right)^2, \tag{34}$$

and $y_m$ for $m = 1, 2, \ldots, pM$ are the observed pixel values. Clearly, the cost function in (34) balances two types of errors. The first term on the right hand side is minimized when $\mathbf{z}$, projected through the observation model, matches the observed data. However, direct minimization of this term can lead to excessive noise magnification due to the ill-posed nature of the inverse problem. Thus, the second term serves as a regularization operator. The parameters $\alpha_{i,j}$ are generally selected so that the regularization term is minimized when $\mathbf{z}$ is smooth. Here we select $\alpha_{i,j}$ to be $1/4$ only for those four values of $j$ which correspond to immediate spatial neighbors of $z_i$. The others are set to zero. The weight of these competing "forces" in the cost function is controlled by the "tuning" parameter $\lambda$. Larger values of $\lambda$ will generally lead to a smoother solution. This is useful when only a small number of frames is available or the fidelity of the observed data is low. It is also possible to make $\lambda$ spatially adaptive in a fashion similar to that in [20, 21]. Finally, note that the estimate defined in (33) and (34) can be viewed as MAP estimate in the case of Gaussian noise and where $\mathbf{z}$ is a realization of a Gauss-Markov random process [13].

Next we consider two unconstrained optimization techniques for minimizing the cost function in (34). First we consider a gradient descent approach and then we present a conjugate gradient method.

## 4.1 Gradient Descent Optimization

To derive the gradient descent update procedure for the image estimate, we begin by differentiating (34) with respect to some pixel $z_k$ for $k = 1, 2, \ldots, N$. This partial derivative is given by

$$g_k(\mathbf{z}) = \frac{\partial C(\mathbf{z})}{\partial z_k} = \sum_{m=1}^{pM} w_{m,k} \left[ \sum_{r=1}^{N} w_{m,r} z_r - y_m \right] \tag{35}$$
$$+ \lambda \left( z_k - \sum_{j=1}^{N} \alpha_{k,j} z_j + \sum_{i=1}^{N} \alpha_{i,k} \left[ \sum_{j=1}^{N} \alpha_{i,j} z_j - z_i \right] \right).$$

The iterative procedure begins with an initial estimate of the high resolution image $\hat{\mathbf{z}}^0$. A relatively simple starting point can be obtained by interpolating the first frame using bilinear or bicubic interpolation. The gradient descent update for each pixel estimate is

$$\hat{z}_k^{n+1} = \hat{z}_k^n - \varepsilon^n g_k(\hat{\mathbf{z}}^n), \tag{36}$$

for $n = 0, 1, 2, \ldots$ and $k = 1, 2, \ldots, N$. Alternatively, the update can be written as

$$\hat{\mathbf{z}}^{n+1} = \hat{\mathbf{z}}^n - \varepsilon^n \mathbf{g}^n, \tag{37}$$

where

$$\mathbf{g}^n = \begin{bmatrix} g_1(\hat{\mathbf{z}}^n) \\ g_2(\hat{\mathbf{z}}^n) \\ \vdots \\ g_N(\hat{\mathbf{z}}^n) \end{bmatrix}. \tag{38}$$

The parameter $\varepsilon^n$ in (36) and (37) represents the step size at the $n$'th iteration. This parameter must be selected to be small enough to prevent divergence and large enough to provide convergence in a reasonable number of iterations. The optimal step size can be calculated by minimizing

$$C(\hat{\mathbf{z}}^{n+1}) = C(\hat{\mathbf{z}}^n - \varepsilon^n \mathbf{g}^n) \tag{39}$$

with respect to $\varepsilon^n$. To do so we begin by writing $C(\hat{\mathbf{z}}^{n+1})$ using (34) and (36). Next we differentiate this with respect to $\varepsilon^n$ and set the derivative equal to zero. Solving for $\varepsilon^n$ yields, after some manipulation,

$$\varepsilon^n = \frac{\sum_{m=1}^{pM} \gamma_m \left( \sum_{r=1}^{N} w_{m,r} \hat{z}_r^n - y_m \right) + \lambda \sum_{i=1}^{N} \bar{g}_i \left( \hat{z}_i^n - \sum_{j=1}^{N} \alpha_{i,j} \hat{z}_j^n \right)}{\sum_{m=1}^{pM} \gamma_m^2 + \lambda \sum_{i=1}^{N} \bar{g}_i^2}, \tag{40}$$

16

Table 2: Proposed gradient descent iterative estimation algorithm.

**step 1**: Begin at $n = 0$ with initial estimate $\hat{\mathbf{z}}^0$ being the interpolated low resolution frame 1.

**step 2**: Compute the gradient $g_k(\hat{\mathbf{z}}^n)$ given in (35) for $k = 1, 2, \ldots, N$, yielding $\mathbf{g}^n$.

**step 3**: Compute the optimal step size $\varepsilon^n$ using (40).

**step 4**: Let $\hat{\mathbf{z}}^{n+1} = \hat{\mathbf{z}}^n - \varepsilon^n \mathbf{g}^n$.

**step 5**: If $||\hat{\mathbf{z}}^{n+1} - \hat{\mathbf{z}}^n|| / ||\hat{\mathbf{z}}^n|| < T$, let $\hat{\mathbf{z}} = \hat{\mathbf{z}}^{n+1}$ and stop.

**step 6**: Let $n = n + 1$ and go to step 2.

where

$$\gamma_m = \sum_{r=1}^{N} w_{m,r} g_r(\hat{\mathbf{z}}^n) \tag{41}$$

is the gradient projected through the model, and

$$\bar{g}_i = g_i(\hat{\mathbf{z}}^n) - \sum_{j=1}^{N} \alpha_{i,j} g_j(\hat{\mathbf{z}}^n) \tag{42}$$

is $g_i(\hat{\mathbf{z}}^n)$ minus the weighted sum of its "neighbors." This iteration continues until the cost function stabilizes or $||\hat{\mathbf{z}}^{n+1} - \hat{\mathbf{z}}^n|| / ||\hat{\mathbf{z}}^n|| < T$, where $T$ is a specified threshold value. A summary of the gradient descent optimization procedure is provided in Table 2.

## 4.2 Conjugate Gradient Optimization

In this section, we describe a conjugate gradient optimization procedure for minimizing the cost function in (34). In particular, we employ the Fletcher-Reeves method [22]. We later show that with little additional computational complexity, faster convergence can be achieved using this method compared to gradient descent.

The basic conjugate gradient image update is given by

$$\hat{z}_k^{n+1} = \hat{z}_k^n + \varepsilon^n d_k(\hat{\mathbf{z}}^n), \tag{43}$$

for $n = 0, 1, 2, \ldots$ and $k = 1, 2, \ldots, N$. Here $d_k(\hat{\mathbf{z}}^n)$ is the conjugate gradient term. Alternatively, the update can be written as

$$\hat{\mathbf{z}}^{n+1} = \hat{\mathbf{z}}^n + \varepsilon^n \mathbf{d}^n, \tag{44}$$

where

$$\mathbf{d}^n = \begin{bmatrix} d_1(\hat{\mathbf{z}}^n) \\ d_2(\hat{\mathbf{z}}^n) \\ \vdots \\ d_N(\hat{\mathbf{z}}^n) \end{bmatrix}. \tag{45}$$

As before, the parameter $\varepsilon^n$ is the step size at the $n$'th iteration. The optimal step size can be calculated by minimizing $C(\hat{\mathbf{z}}^{n+1}) = C(\hat{\mathbf{z}}^n + \varepsilon^n \mathbf{d}^n)$ with respect to $\varepsilon^n$. This yields

$$\varepsilon^n = -\frac{\sum_{m=1}^{pM} \phi_m \left( \sum_{r=1}^{N} w_{m,r} \hat{z}_r^n - y_m \right) + \lambda \sum_{i=1}^{N} \bar{d}_i \left( \hat{z}_i^n - \sum_{j=1}^{N} \alpha_{i,j} \hat{z}_j^n \right)}{\sum_{m=1}^{pM} \phi_m^2 + \lambda \sum_{i=1}^{N} \bar{d}_i^2}, \tag{46}$$

where

$$\phi_m = \sum_{r=1}^{N} w_{m,r} d_r(\hat{\mathbf{z}}^n) \tag{47}$$

and

$$\bar{d}_i = d_i(\hat{\mathbf{z}}^n) - \sum_{j=1}^{N} \alpha_{i,j} d_j(\hat{\mathbf{z}}^n). \tag{48}$$

The conjugate gradient vector is initially set to be

$$\mathbf{d}^0 = -\mathbf{g}^0. \tag{49}$$

This is updated according to

$$\mathbf{d}^{n+1} = -\mathbf{g}^{n+1} + \beta^n \mathbf{d}^n, \tag{50}$$

where

$$\beta^n = \frac{(\mathbf{g}^{n+1})^T \mathbf{g}^{n+1}}{(\mathbf{g}^n)^T \mathbf{g}^n}. \tag{51}$$

Again, the iterations continue until the estimate converges. A summary of the conjugate gradient optimization procedure is given in Table 3.

Table 3: Proposed conjugate gradient iterative optimization algorithm.

---

**step 1**: Begin at $n = 0$ with initial estimate $\hat{\mathbf{z}}^0$ being the interpolated low resolution frame 1.

**step 2**: Compute $\mathbf{g}^0$ and initialize conjugate gradient vector as $\mathbf{d}^0 = -\mathbf{g}^0$.

**step 3**: Compute the optimal step size $\varepsilon^n$ using (46).

**step 4**: Let $\hat{\mathbf{z}}^{n+1} = \hat{\mathbf{z}}^n + \varepsilon^n \mathbf{d}^n$.

**step 5**: If $||\hat{\mathbf{z}}^{n+1} - \hat{\mathbf{z}}^n|| / ||\hat{\mathbf{z}}^n|| < T$, let $\hat{\mathbf{z}} = \hat{\mathbf{z}}^{n+1}$ and stop.

**step 6**: Compute $\mathbf{g}^{n+1}$ and let $\mathbf{d}^{n+1} = -\mathbf{g}^{n+1} + \beta^n \mathbf{d}^n$, where $\beta^n = \frac{(\mathbf{g}^{n+1})^T \mathbf{g}^{n+1}}{(\mathbf{g}^n)^T \mathbf{g}^n}$.

**step 7**: Let $n = n + 1$ and go to step 3.

---

# 5 Experimental Results

In this section a number of experimental results are presented in order to demonstrate the performance of the proposed algorithm. The first set of experiments involve simulated data derived from a single broad band visible image. The second set of results use data obtained from a real-time FLIR imaging system.

## 5.1 Simulated Imagery

Here we use simulated data in order to evaluate the algorithms quantitatively. In particular, 16 low resolution images are generated by rotating, translating, blurring and subsampling an "ideal" image. The rotation and translation parameters for each frame have been selected arbitrarily and are shown in Fig. 6. The original image is of size $250 \times 250$ and the down sampling factors are $L_1 = L_2 = 5$. The blurring function is a $5 \times 5$ moving average filter, which simulates the low resolution detector effects. Finally, additive Gaussian noise of variance $\sigma_\eta^2 = 10$ is introduced in each frame. The estimated registration parameters, using the algorithm in Table 1, are also shown in Fig.
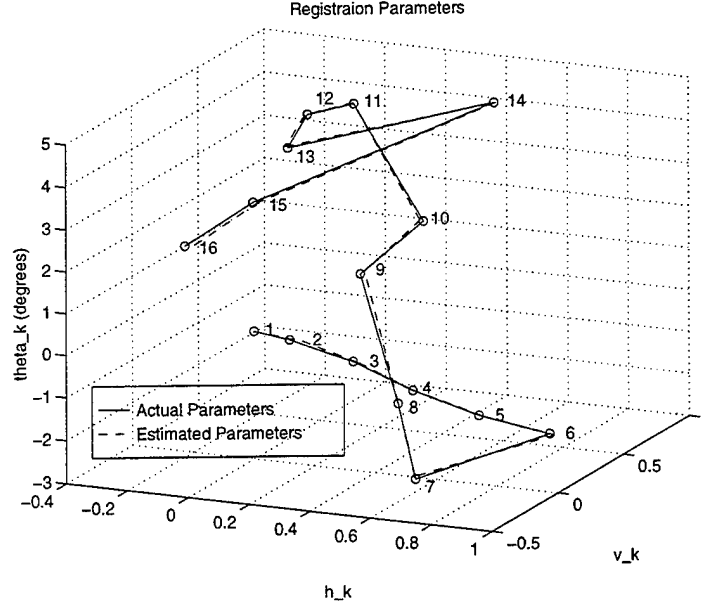
Figure 6: Actual and estimated registration parameters for each of the 16 simulated low resolution frames. The shifts $h_k$ and $v_k$ are measured in terms of low resolution pixel spacings.

6. The mean absolute error (MAE) between the actual and estimated translational shifts is 0.0414 low resolution pixel spacings and the MAE for the rotation parameters is 0.0250 degrees.

The original 8 bit grayscale image "Aerial" is shown in Fig. 7(a). One typical frame of the simulated low-resolution noisy data is shown in Fig. 7(b). The multi-frame image estimate, using the estimated registration parameters, is shown in Fig. 7(c). The initial image estimate used here is a bilinearly interpolated version of the first frame. Twenty iterations of the conjugate gradient optimization have been performed with $\lambda = 0.1$. We find that the algorithm is not highly sensitive to the choice of $\lambda$. For comparison with the multi-frame estimate, a bicubic interpolation of the single frame in Fig. 7(b) is shown in Fig. 7(d).

To show the convergence behavior of the gradient descent and conjugate gradient procedures, the values of the cost function in (34) are plotted in Fig. 8 versus iteration number for each. Note that the conjugate gradient method shows superior convergence speed. The MAE between the multi-frame estimate and the "ideal" image is plotted in Fig. 9 as a function of the number of frames used. For comparison, the MAEs
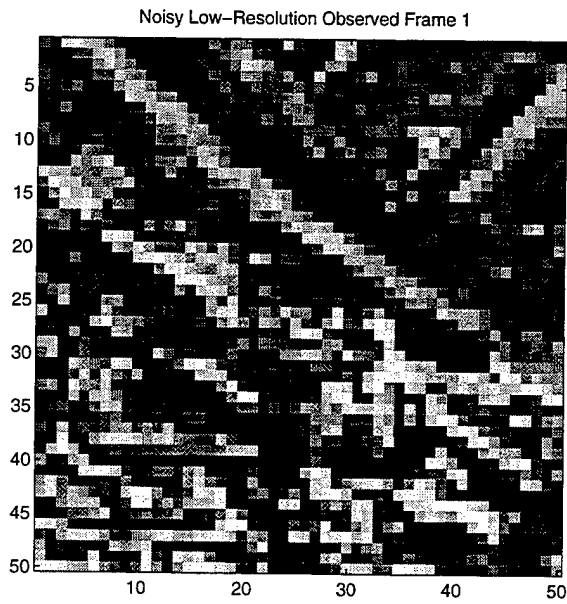
20

Original Image Aerial



(a)

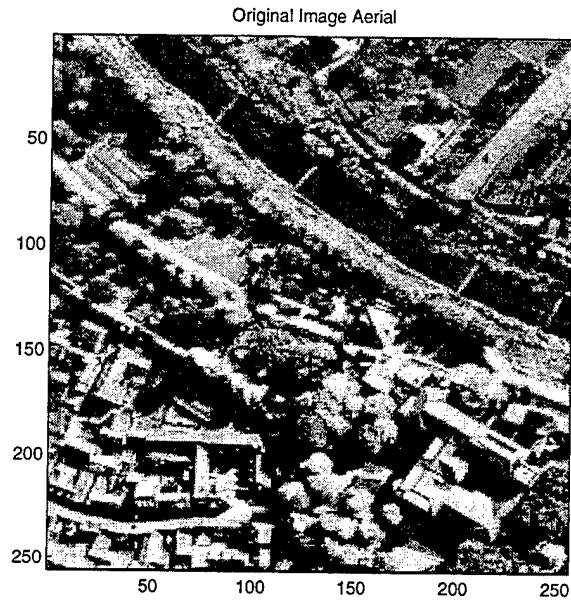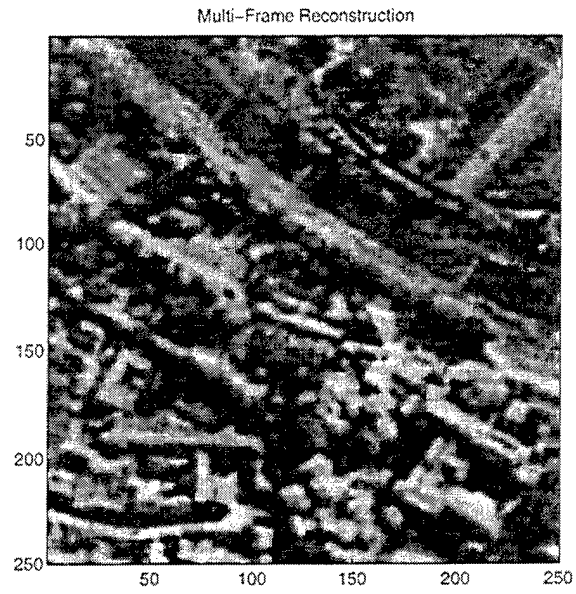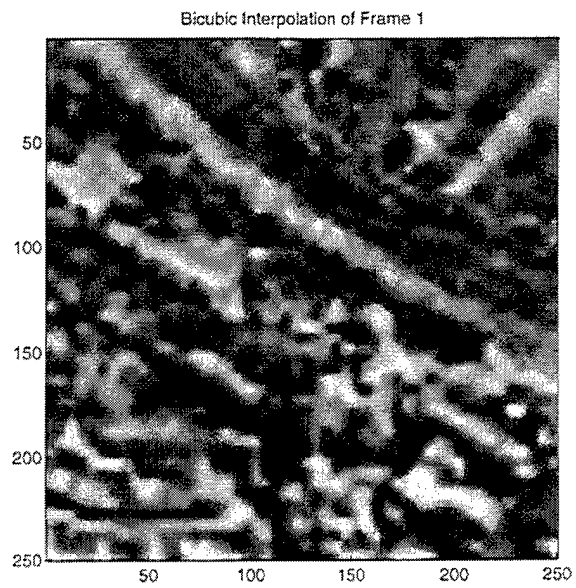Noisy Low–Resolution Observed Frame 1



(b)

Figure 7: (a) Original image "Aerial" (b) simulated low resolution frame 1 where $L_1 = L_2 = 5$ and $\sigma_\eta^2 = 10$ (c) multi-frame image estimate using 16 frames with $\lambda = 0.1$ (d) bicubic interpolation of frame 1.

21

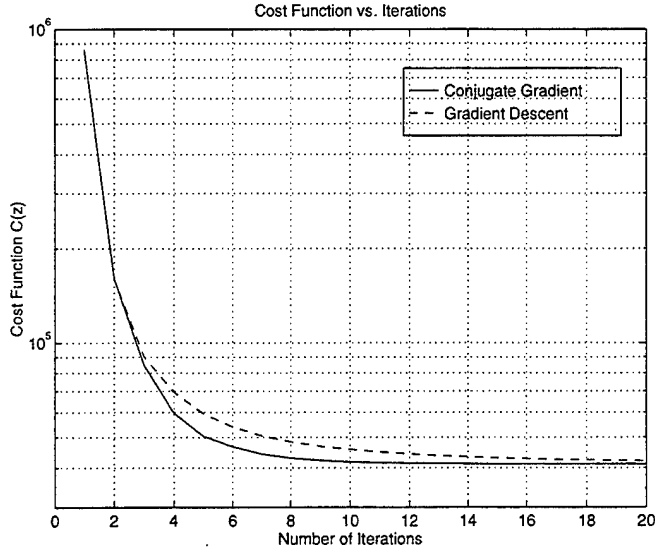Multi-Frame Reconstruction

(c)



Bicubic Interpolation of Frame 1

(d)

Figure 8: Convergence behavior of the gradient descent and conjugate gradient procedures using the 16 frames of simulated data. The noise variance is $\sigma_\eta^2 = 10$ and $\lambda = 0.1$.

of the first frame bilinearly and bicubically interpolated are also shown. With only one frame, the proposed algorithm's performance is only slightly better than that of the bicubic interpolator. However, with additional frames, the estimate becomes significantly improved with respect to the single frame interpolators. Similar results are observed with mean squared error.

## 5.2  FLIR Imagery

Now we consider applying the multi-frame algorithm to FLIR data from the imager described in Section 2.3. We have chosen to perform a reconstruction with $L_1 = L_2 = 5$, although this resolution may not be sufficient to avoid aliasing effects entirely. The theoretical discrete PSF of the FLIR system on the high resolution grid, given by (12), is shown in Fig. 10.

The multi-frame algorithm is tested using 20 frames of the FLIR imagery. The frames have been acquired at a 60 frame per second rate. The rotation and translation is introduced by arbitrarily manipulating the imager during acquisition. One typical original resolution frame is shown in Fig. 11(a). This $80 \times 80$ image represents a region of interest from the full $128 \times 128$ Amber array. The scene contains a number of small power boats
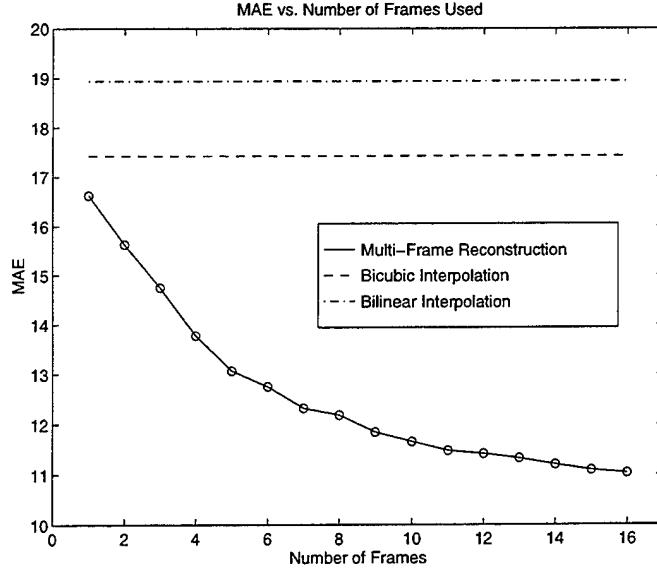
23

Figure 9: Mean absolute error for the multi-frame estimator using different numbers of frames. The noise variance is $\sigma_\eta^2 = 10$ and $\lambda = 0.1$.

and trailers on a gravel parking lot with a fence in the foreground. The multi-frame estimate is shown in Fig. 11(b) for $\lambda = 0.1$. Again, the initial image estimate is obtained by bilinearly interpolating the first frame and 10 iterations of the conjugate gradient procedure have been performed. For comparison, a bilinearly interpolated single frame is shown in Fig. 11(c). A bicubically interpolated version of the single frame is shown in Fig. 11(d). The multi-frame reconstruction appears to show significantly improved image detail. In addition, note that the aliasing artifacts on the diagonal beam of the gate in the foreground of Figs. 11(a), 11(c) and 11(d) are virtually eliminated in the multi-frame estimate. The estimated registration parameters for the 20 observed frames are shown in Fig. 12.

Finally, to illustrate the convergence behavior of the algorithms using the FLIR data, the cost function is plotted in Fig. 13 versus iteration number for both the gradient descent and the conjugate gradient optimization methods. Again, the conjugate gradient algorithm exhibits slightly faster convergence.
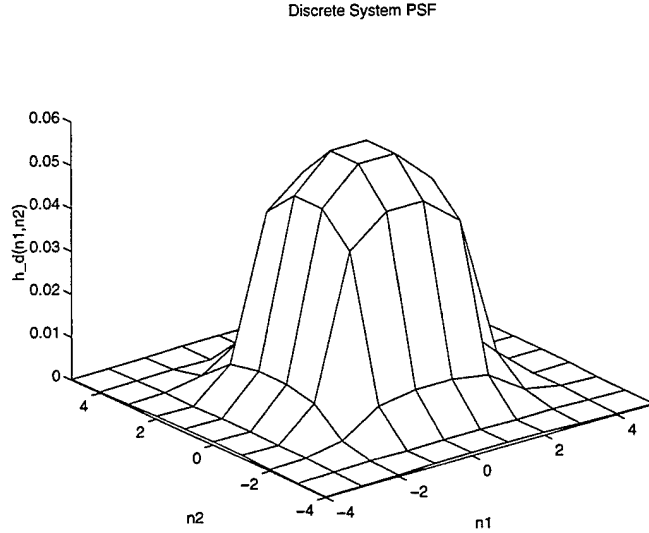
24

Figure 10: Theoretical discrete system PSF of the FLIR imager for $L_1 = L_2 = 5$.

# 6 Conclusions

Aliasing reduction and resolution enhancement can be achieved by exploiting multiple frames which are rotated and/or translated with respect to one another. This is possible because each frame offers a unique set of discrete samples. For an imager mounted on a moving platform, such as an aircraft, the desired image sequence may arise from natural line-of-sight jitter and rotation of the platform. With this in mind, it may then be possible to relax image stabilization requirements in some applications and obtain improved resolution images through the proposed algorithm. The tradeoff here is that of temporal resolution for spatial resolution. That is, multiple low resolution frames are required to form each new high resolution image.

The key to the success of the algorithm is having an accurate observation model. This includes the image registration parameters and the system PSF. The observation model proposed here includes accurate information about the optical system. We believe that this provides a reasonably accurate system PSF. A regularized cost function defines the image estimate. Minimization of the cost function is performed using either a gradient descent or conjugate gradient technique.

The quantitative results obtained show that the multi-frame image estimates have significantly lower error than estimates formed by single frame interpolation. Furthermore,
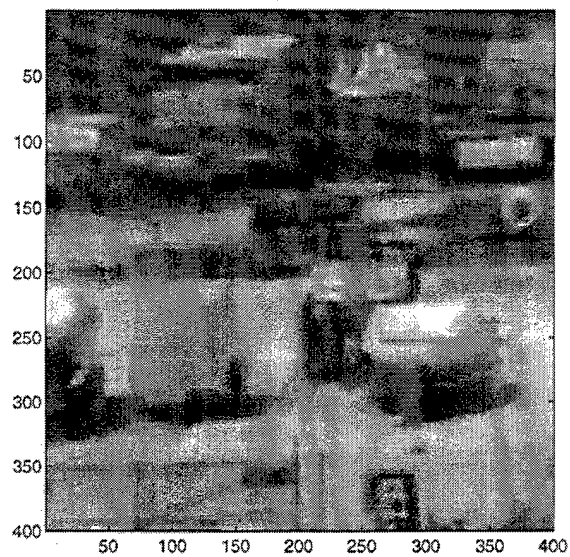
Low Resolution Frame 1

(a)

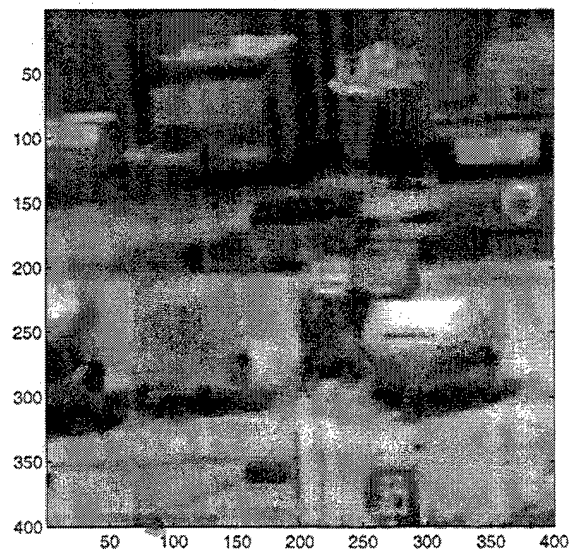

Multi-Frame Reconstructed Image
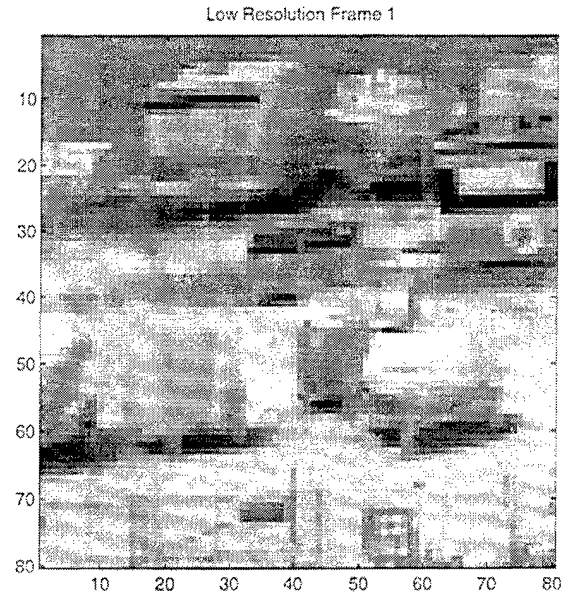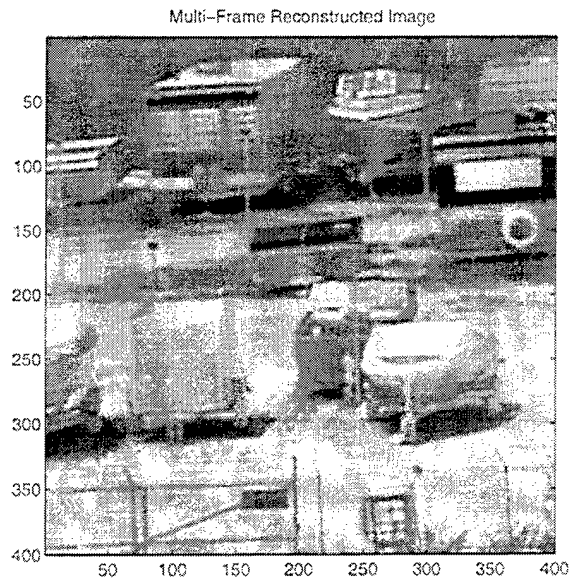
(b)

Figure 11: (a) FLIR low resolution frame 1 showing small power boats and trailers on a gravel parking lot (b) multi-frame estimate using 20 frames with $L_1 = L_2 = 5$ and $\lambda = 0.1$ (c) bilinear interpolation of frame 1 (d) bicubic interpolation of frame 1.

Bilinear Interpolation of Frame 1

(c)



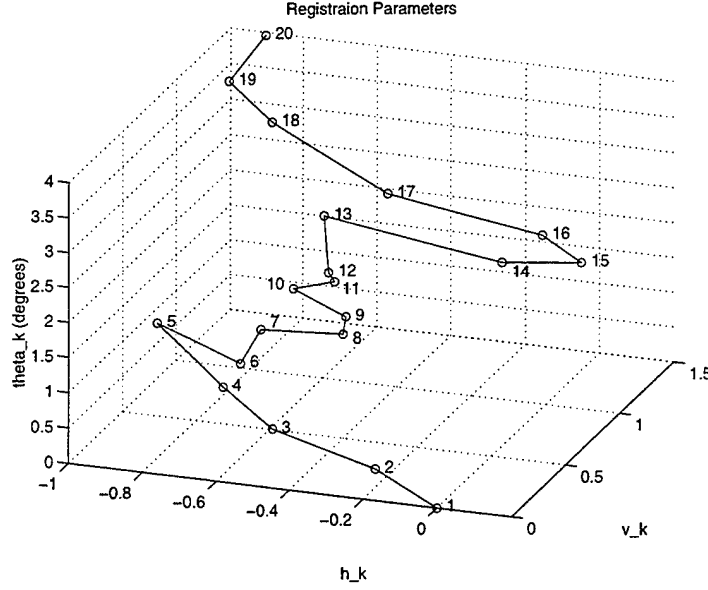Bicubic Interpolation of Frame 1

(d)

27

Figure 12: Estimated registration parameters for the 20 frames acquired with the FLIR imager.

we believe that the FLIR results show that the multi-frame estimate has significantly improved image detail. In particular, edges and fine structure emerge in the multi-frame reconstruction that are not visible in the low resolution data. Because these features offer important visual cues, we believe that the utility of the processed image is greatly enhanced.
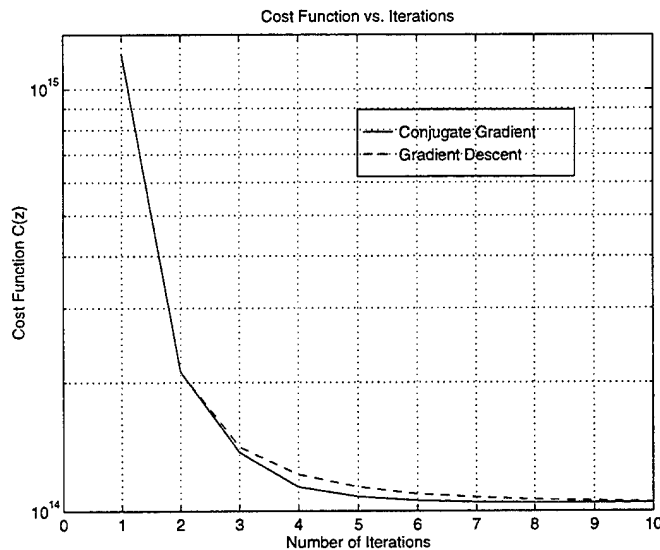
# 7 Acknowledgments

28

Figure 13: Convergence behavior of the gradient descent and conjugate gradient optimization techniques using the FLIR data. Twenty observed frames have been used with $L_1 = L_2 = 5$ and $\lambda = 0.1$.

Barnard, and Bill Martin for their helpful feedback and comments. Thanks are also due to Tony Absi and Art Serrano for their administrative support. Finally, we would like to gratefully acknowledge the work of those FLIR team members who support the hardware and software which made this work possible, Bob Gualtieri, Rich Hill, Al Meyer, Joe Richardson, Carl White and Ron Wiensch.

# References

[1] J. C. Gillette, T. M. Stadtmiller, and R. C. Hardie, "Reduction of aliasing in staring infrared imagers utilizing subpixel techniques," *Optical Engineering*, vol. 34, Nov. 1995.

[2] E. A. Watson, R. A. Muse, and F. P. Blommel, "Aliasing and blurring in microscanned imagery," in *SPIE Infrared Imaging Systems: Design, Analysis, Modeling and Testing III*, vol. 1689, Apr. 1992.

[3] R. Tsai and T. Huang, "Multiframe image restoration and registration," in *Advances in Computer Vision and Image Processing*, vol. 1, JAI Press Inc., 1984.

[4] S. Kim, N. Bose, and H. Valenzuela, "Recursive reconstruction of high resolution image from noisy undersampled multiframes," *IEEE Transactions on Acoustics, Speech, and Signal Processing*, vol. 38, June 1990.

[5] S. Kim, , and W.-Y. Su, "Recursive high-resolution reconstruction of blurred multiframe image," *IEEE Transactions on Acoustics, Speech and Signal Processing*, vol. 2, Oct. 1993.

[6] H. Stark and P. Oskoui, "High-resolution image recovery from image-plane arrays, using convex projections," *Journal of the Optical Society of America A*, vol. 6, no. 11, 1989.

[7] A. Patti, M. Sezan, and A. Tekalp, "High-resolution image reconstruction from a low-resolution image sequence in the presence of time-varying motion blur," in *Proceedings of IEEE International Conference on Image Processing, Austin, TX*, Nov. 1994.

[8] A. Patti, M. Sezan, and A. Tekalp, "High-resolution standards conversion of low resolution video," in *Proceedings of IEEE International Conference on Acoustics, Speech and Signal Processing (ICASSP), Detroit, MI*, May 1995.

[9] R. R. Schultz and R. L. Stevenson, "Extraction of high-resolution frames from video sequences," in *IEEE International Conference on Acoustics, Speech and Signal Processing (ICASSP), Detroit MI*, May 1995.

[10] R. R. Schultz and R. L. Stevenson, "Extraction of high-resolution frames from video sequences," *IEEE Transactions on Image Processing*, vol. 5, June 1996.

[11] R. R. Schultz and R. L. Stevenson, "A baysian approach to image expansion for improved definition," *IEEE Transactions on Image Processing*, vol. 3, May 1994.

[12] S. Cain, R. C. Hardie, and E. Armstrong, "Restoration of aliased video sequences via a maximum-likelihood approach," in *National Infrared Information Symposium (IRIS) on Passive Sensors, Monterey, CA*, Mar. 1996.

[13] R. C. Hardie and S. Cain, "Map estimation of a high resolution image from a sequence of undersampled translationally shifted frames," *Submitted to IEEE Transactions on Image Processing*, Feb. 1996.

[14] P. Cheeseman, B. Kanefsky, R. Kraft, J. Stutz, and R. Hanson, "Super-resolved surface reconstruction from multiple image," *NASA Technical Report FIA-94-12*, Dec. 1994.

[15] M. Irani and S. Peleg, "Improving resolution by image registration," *CVGIP: Graphical Models and Image Processing*, vol. 53, May 1991.

[16] A. K. Jain, *Fundamentals of Digital Image Processing*. Prentice Hall, 1989.

[17] J. Goodman, *Introduction to Fourier Optics*. Mcgraw-Hill, 1968.

[18] A. V. Oppenheim and R. W. Schafer, *Discrete-Time Signal Processing*. Prentice Hall, 1989.

[19] B. D. Lucas and T. Kanade, "An iterative image registration technique with an application to stereo vision," in *International Joint Conference on Artificial Intelligence, Vancouver*, Aug. 1981.

[20] Y.-L. You and M. Kaveh, "A regularized approach to joint blur identification and image restoration," *IEEE Transactions on Image Processing*, vol. 5, Mar. 1996.

[21] R. L. Lagendijk, J. Biemond, and D. E. Boekee, "Regularized iterative image restoration with ringing reduction," *IEEE Transactions on Acoustics, Speech, and Signal Processing*, vol. 36, Dec. 1988.

[22] D. G. Luenberger, *Linear and Nonlinear Programming*. Addison-Wesley, 1984.